



# Local microenvironment modulation of $\text{Pt}^0/\text{Pt}^{2+}$ nano-clusters inducing synchronous mass transfer effect to boost catalytic ozonation

Tao Zhong <sup>a</sup>, Xianhu Long <sup>a</sup>, Manhui Luo <sup>a</sup>, Su Tang <sup>a</sup>, Wenbin Huang <sup>a</sup>, Huinan Zhao <sup>a,\*</sup>,<sup>1</sup>, Lingling Hu <sup>a</sup>, Shuanghong Tian <sup>a</sup>, Dong Shu <sup>b</sup>, Chun He <sup>a,\*</sup>

<sup>a</sup> School of Environmental Science and Engineering, Sun Yat-sen University, Guangzhou 510275, China

<sup>b</sup> School of Chemistry, South China Normal University, Guangzhou 510006, China



## ARTICLE INFO

### Keywords:

$\text{Pt}^0/\text{Pt}^{2+}$

Microenvironment

Interfacial diffusion

Synchronous mass transfer

Catalytic ozonation

S-VOCs

## ABSTRACT

Rational catalyst structure design is expected to solve the low  $\text{O}_3$  utilization and poor molecular mass transfer efficiency in heterogeneous catalytic ozonation (HCO). Herein, Pt/CMK-3 catalyst with confined space to enhance mass transfer was synthesized and employed for  $\text{CH}_3\text{SH}$  removal. Unlike fully free diffusion in 0–2.0 wt % Pt/CMK-3 and bulk phase diffusion in 10.0 wt % Pt/CMK-3, removal efficiency of 5.0 wt % Pt/CMK-3 was significantly improved to 97.0%, which was attributed to the effective interfacial diffusion of  $\text{O}_3$  and  $\text{CH}_3\text{SH}$  through local microenvironment modulation of  $\text{Pt}^0/\text{Pt}^{2+}$  nanoclusters (NCs) inducing synchronous mass transfer. Experimental and DFT calculations confirmed the strong electronic interactions between  $\text{O}_3$  and  $\text{Pt}^0$  facilitated charge redistribution and preferential  $\text{O}_3$  activation. AIMD simulation demonstrated that the synchronous difference in mean-square displacements (MSD) and diffusion coefficient (Dc) of  $\text{CH}_3\text{SH}$  ( $\text{Dc}=0.022$ ) and  $\text{O}_3$  ( $\text{Dc}=0.0046$ ) in the confined Pt/CMK-3 system could facilitate  $\text{CH}_3\text{SH}$  migrate to  $\text{Pt}^{2+}$  through interfacial diffusion. Especially, the d-orbital electrons of Pt NCs interact sequentially with p-orbital electrons of  $\text{CH}_3\text{SH}$  and  $\text{O}_3$  to maintain redox of  $\text{Pt}^0/\text{Pt}^{2+}$ . This study provides novel insights on effective mass transfer and kinetic properties of gaseous reaction between oxidant and pollutant by constructing unique interfacial diffusion behaviors.

## 1. Introduction

Sulfur-containing volatile organic compounds (S-VOCs) emitted into atmosphere are one of the most important potential precursor gaseous pollutants contributing to formation of ozone ( $\text{O}_3$ ), photochemical smog, and urban haze etc. [1,2]. Specially, the ambient concentration limit for methyl mercaptan ( $\text{CH}_3\text{SH}$ , a typical S-VOCs odor gas) is 0.002 mg/m<sup>3</sup>, which is much stricter than the concentration limit of  $\text{H}_2\text{S}$  (0.02 mg/m<sup>3</sup>) and  $\text{C}_2\text{H}_6\text{S}$  (0.02 mg/m<sup>3</sup>) [3]. Therefore, the harmless treatment of S-VOCs has attracted extensive attention of the scientific community.

Currently, heterogeneous catalytic ozonation (HCO) technology can effectively remove  $\text{CH}_3\text{SH}$  at room temperature or under complex environment conditions [4–6]. Nonetheless, the accumulation of sulfur-containing intermediates on the surface of metal-containing catalysts lead to catalyst deactivation. And the byproducts may compete with  $\text{O}_3$  for adsorption, hindering the efficient utilization of  $\text{O}_3$  and

resulting in slow mass transfer in practical applications [7]. How to improve the utilization efficiency of  $\text{O}_3$  while ensuring the effective removal of  $\text{CH}_3\text{SH}$  has become one of the challenges in HCO technology.

The effective mass transfer of  $\text{O}_3$  and  $\text{CH}_3\text{SH}$  has great potential in promoting the kinetics of catalytic reactions. It can be imagined that the diffusion of  $\text{O}_3$  and  $\text{CH}_3\text{SH}$  at the catalyst surface/interface will lead to mass transfer differences [8], and the ideal effective mass transfer determined by characterization can maximize the utilization of  $\text{O}_3$  to generate large number of reactive oxygen species (ROSs) [9,10]. In contrast, if the mass transfer and diffusion of  $\text{O}_3$  and  $\text{CH}_3\text{SH}$  are quite ineffective, this will result in the quenching of ROSs generated by  $\text{O}_3$  (due to the lifespan of ROSs typically being a few picoseconds) [11,12], and ultimately lead to lower catalytic activity as well as catalyst reduction of catalyst active sites. However, it is currently unclear whether the effective mass transfer implies simultaneous diffusion of  $\text{O}_3$  and  $\text{CH}_3\text{SH}$  to the active reaction site at the same time, or whether  $\text{O}_3$  and  $\text{CH}_3\text{SH}$  sequentially and synchronously diffuse to different active

\* Corresponding authors.

E-mail addresses: [zhaohn@mail2.sysu.edu.cn](mailto:zhaohn@mail2.sysu.edu.cn) (H. Zhao), [hechun@mail.sysu.edu.cn](mailto:hechun@mail.sysu.edu.cn) (C. He).

<sup>1</sup> ORCID: 0000-0002-3875-5631

site. In this case, by designing an appropriate active metal anchored to the support matrix with confined space, and modulating their local microenvironments to control the regulation of molecular diffusion behavior, it could achieve  $O_3$  activation and highly effective  $CH_3SH$  removal in confined space [13].

Recently, ordered mesoporous carbon nanotubes (OM-CNTs) are widely concerned due to their stable chemical properties, special channel structure, large specific surface area and good dispersion of metal catalysts [14]. Therefore, the combination of Pt nanoclusters (NCs) with OM-CNTs can efficiently control the local microenvironment of the catalytic reaction, leading to an enhancement in the local electron density surrounding the metal atoms and influencing the electron filling of the  $e_g$  orbitals. This is crucial for both the thermodynamic and kinetic aspects of the surface reaction [15]. Furthermore, the Pt-C interfacial layers presented in the confined meso-channels of OM-CNTs provides a free-moving channel for the inward  $O_3$  and  $CH_3SH$  [16]. Predictably, OM-CNTs could effectively improve the activity and durability of metal-based catalysts used as protective shells, and provide confined space for promoting charge/mass transfer for generating more ROSs [15].

Herein, a novel Pt/CMK-3 model catalyst with confined channel was synthesized by coupling EMSI and confined effect between Pt NCs and CMK-3 for removal  $CH_3SH$ . Due to the existence of different valence states of Pt (i.e.,  $Pt^0$  and  $Pt^{2+}$ ) in Pt NCs,  $Pt^0$  can effectively activate  $O_3$ , while  $Pt^{2+}$  is more conducive to the adsorption of  $CH_3SH$ . The activation mechanism of  $O_3$  and the degradation pathway of  $CH_3SH$  during HCO process were revealed by in-situ Raman, in-situ DRIFTS, and PTR-TOF-MS analysis. DFT calculations and AIMD simulations were used to gain a deeper insight on the electronic interactions between  $O_3$ ,  $CH_3SH$  and catalysts as well as the mass transfer behavior. This work will pave the way for the rational design of catalysts in confinement systems for environmental applications by constructing a confined interfacial diffusive behavior for effective mass transfer between oxidants and S-VOCs molecules.

## 2. Experimental details

### 2.1. Preparation of catalysts

Synthesis of Pt/CMK-3: 3.32 mL  $H_2PtCl_6 \cdot 6 H_2O$  (4 mg  $mL^{-1}$ ) was added into 60 mL deionized water and stirred 0.5 h. Then, 100 mg CMK-3 was added to the mixed solution and followed by continuous stirring for 12 h at ambient temperature. After that, excess of  $NaBH_4$  (0.1 M) was added to the solution, and reduced for 3 h under ice bath, then washed with a large amount of deionized water. Finally, the solid powder was dried at 60 °C for 8 h. The obtained material denoted as Pt/CMK-3. For comparison, the preparation of Pt/C-Si only changes the substrate material to C-Si, and the rest of the preparation process is the same as above.

More detailed information was provided in Text S2.

### 2.2. Catalytic ozonation removal of $CH_3SH$

The removal of  $CH_3SH$  was measured in a continuous-flow cylindrical stainless steel microreactor (i.d. width = 8 mm; length = 490 mm) with 30.0 mg of catalyst under ambient temperature and atmospheric pressure (Scheme S1).  $CH_3SH$  concentrations were detected by the  $CH_3SH$  sensor (Detcon, DM-400IS), and the inlet  $CH_3SH$  concentration was kept 50 ppm. The total flow rate of feed gas was controlled at 100  $mL \cdot min^{-1}$  using the mass flow controllers (HORIBA METRON), corresponding to gas hourly space velocity (GHSV) equal to 200,000  $mL \cdot h^{-1} \cdot g^{-1}$ . The  $CH_3SH$  removal rate ( $\eta$ ) was calculated as follows [7]:

$$\eta(\%) = \left(1 - \frac{C_t}{C_0}\right) \times 100\% \quad (1)$$

Where  $C_t$ ,  $C_0$  are the concentrations of  $CH_3SH$  in the outlet and feeding streams.

### 2.3. Ab initio molecular dynamics (AIMD) simulations

AIMD simulations were performed using the LAMMPS software. The simulation details were provided in Text S7.

## 3. Results and discussion

### 3.1. Characterization of catalysts

Pt/CMK-3 was prepared by impregnation reduction method (Fig. 1a). CMK-3 exhibited a uniform mesoporous structure (Fig. S1) and Pt NCs were uniformly embedded in the striated channels of CMK-3 (Fig. 1b) with a mean diameter of approximately 3.5 nm and no observable aggregation (Fig. S2a), the lattice spacing was about 0.215 nm (Fig. 1c), corresponding to the (111) facet of  $Pt^0$  [17]. In contrast, Pt NCs loaded on Pt/C-Si formed large size about 5.7 nm (Fig. S2b) due to the larger surface energy for agglomeration (Fig. 1d), and the lattice spacing of Pt (111) was expanded to 0.229 nm (Fig. 1e). The morphology of CMK-3 and Pt/CMK-3 were observed using scanning electron microscopy (SEM) (Fig. S3a, b). Energy dispersive spectrometer (EDS) spectra illustrated the uniform dispersion of Pt, C, and O elements in Pt/CMK-3 (Fig. S3 c-f). The isotherm of C-Si and Pt/C-Si suggested a non-porous structure (Fig. S4a, b). In contrast, the isotherm of CMK-3 and Pt/CMK-3 exhibited a hysteresis loop, indicating type IV isotherms with mesoporous pore structures [18]. The presence of hysteresis loops indicated the formation of numerous mesoporous structures on the CMK-3 surface after HF etching, which was beneficial to the diffusion and adsorption of molecules. Moreover, Pt/CMK-3 had a larger specific surface ( $660.7 \text{ m}^2 \text{ g}^{-1}$ ) area and more evenly dispersed mesopore than Pt/C-Si ( $8.4 \text{ m}^2 \text{ g}^{-1}$ ) (Table S1). The construction of Pt/CMK-3 confined system leads to the occurrence of Knudsen diffusion at suitable concentrations of  $CH_3SH$  and  $O_3$ , which enhances the mass transfer process and improves the catalytic activity [19].

The phase composition of synergized catalysts was investigated by X-ray diffraction (XRD) patterns. CMK-3, C-Si, Pt/CMK-3 and Pt/C-Si had a broad diffraction peak around 23.5° and 43.7°, respectively, corresponding to the stacking of the (002) tubular structure plane and in-plane ordering of (101) facet of graphite carbon [20] (Fig. S5a). In addition, after loading Pt NCs, new diffraction peaks appeared at 39.8°, 46.2° and 67.8° (Fig. S5b), corresponding to the (111), (200) and (220) facet of metal Pt (PDF No. 04-0802) [21]. Furthermore, the model of Pt NCs was established and the fitted XRD pattern was consistent with standard card (Fig. S6). The strongest diffraction peak of (002) obviously shifted to lower angle, indicating that Pt NCs were successfully introduced into the channel of CMK-3. According to Sabatier theory [22], the confinement effect of CMK-3 can effectively prevent the agglomeration of metal during the reduction deposition process, but tend to nucleate and grow slowly and uniformly, which is beneficial to the more sufficient dispersion of metals, exposing more active sites, and ultimately promoting long-term catalytic reaction.

The surface functional groups were analyzed by Fourier transform infrared spectroscopy (FTIR). As depicted in Fig. S7a, the C-O stretching vibration peak at  $1248 \text{ cm}^{-1}$  of Pt/CMK-3 had a slight blue shift compared with CMK-3, which was attributed to the EMSI effect between Pt NCs and CMK-3. C-Si substrate and Pt/C-Si have obvious diffraction peaks at  $1138 \text{ cm}^{-1}$ ,  $958 \text{ cm}^{-1}$  and  $815 \text{ cm}^{-1}$ , which corresponded to Si-O-Si stretching vibration, Si-OH stretching vibration and Si-O symmetric stretching vibration of silicon oxide materials. However, after loading Pt NCs, the infrared characteristic peaks of Pt/C-Si did not shift (Fig. S7b) as the characteristic peak of Pt/CMK-3, indicating a weak interaction between Pt NCs and C-Si substrate, which is not conducive to the uniform dispersion of Pt NCs. Raman spectra (Fig. S8a, b) displayed that the

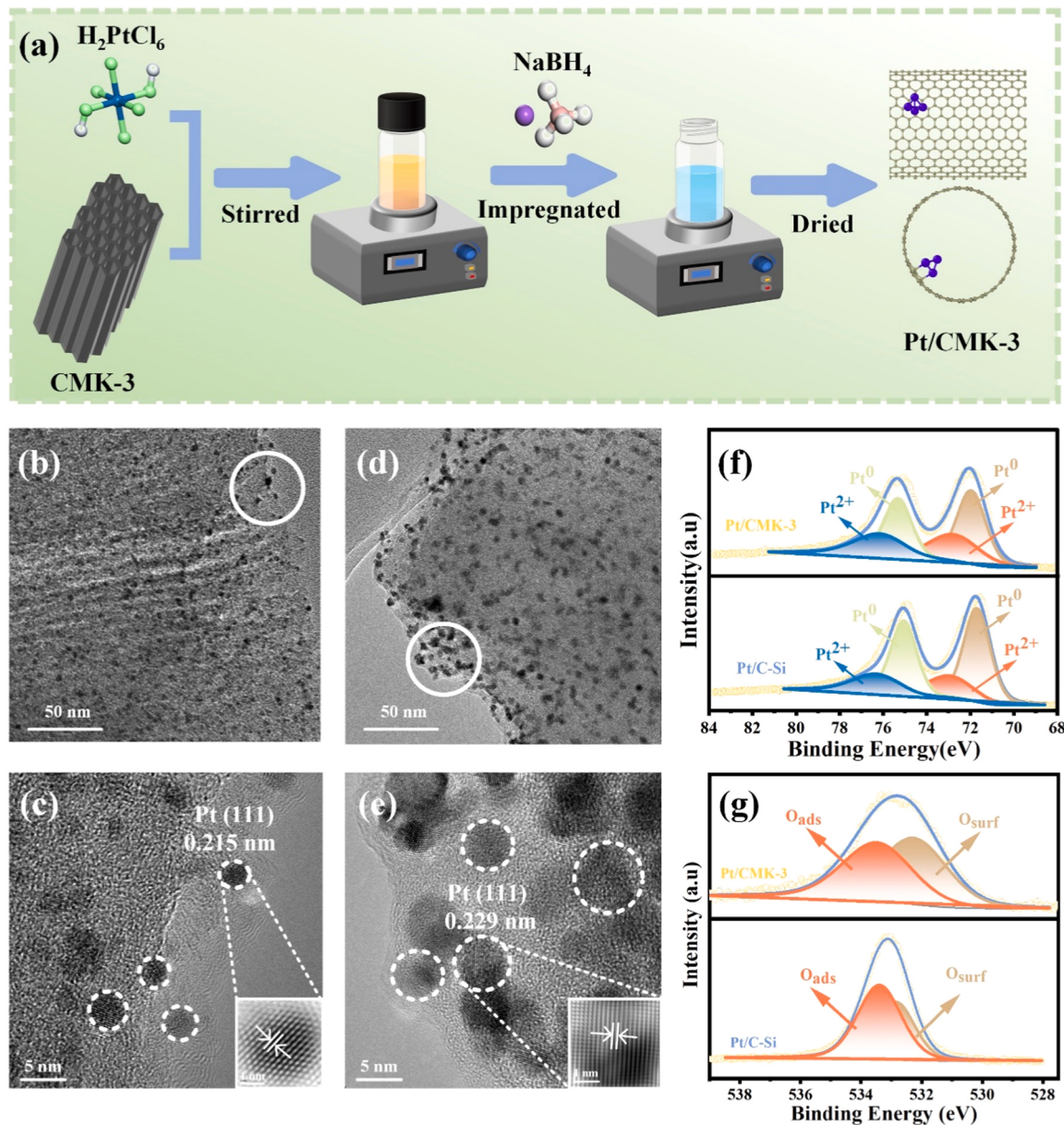


**Fig. 1.** (a) Schematic diagram of Pt/CMK-3 synthesis process; (b) TEM and (c) HR-TEM images of Pt/CMK-3; (d) TEM and (e) HR-TEM images of Pt/C-Si; XPS spectra for (f) Pt 4 f, and (g) O 1 s for Pt/CMK-3 and Pt/C-Si.

peaks at around  $1340\text{ cm}^{-1}$ , designated as the D-band, are associated with the disordered carbon structure; the peaks at approximately  $1585\text{ cm}^{-1}$ , assigned to the G-band, are related to the in-plane vibration of  $\text{sp}^2$  bonded carbon [23]. And the  $I_{\text{D}}/I_{\text{G}}$  value was 1.20 and 1.19 for CMK-3 and C-Si substrate, respectively, confirming that CMK-3 possessed more surface defects. However, after loading Pt NCs, the defect degree of both Pt/CMK-3 ( $I_{\text{D}}/I_{\text{G}} = 1.15$ ) and Pt/C-Si ( $I_{\text{D}}/I_{\text{G}} = 1.14$ ) showed a decreasing tendency. Low-temperature electron paramagnetic resonance (EPR) profiles also confirmed that CMK-3 had more surface defects, whereas Pt/C-Si and Pt/CMK-3 have almost no detectable peaks present (Fig. S9), suggesting that Pt NCs deposited at the surface defect sites of the substrate, and enhanced the interaction between Pt NCs and substrate [24].

The chemical composition and surface value states of catalysts were analyzed by X-ray photoelectron spectroscopy (XPS). The survey spectrum showed that Pt has a weak peak strength in Pt/CMK-3 (Fig. S10a), which may be caused by Pt NCs encapsulated in the pore and/or channel of CMK-3. The C 1 s peak was no significant shift, exhibiting the same

chemical state in Pt/CMK-3 and Pt/C-Si (Fig. S10b). In Fig. 1f, the high-resolution of Pt 4 f can be divided into four peaks at 71.95, 72.80, 75.33, and 76.15 eV, corresponding to Pt 4  $f_{7/2}$  and Pt 4  $f_{5/2}$  orbitals of  $\text{Pt}^0$  and  $\text{Pt}^{2+}$  [25], respectively. The binding energy of  $\text{Pt}^0$  in Pt/CMK-3 was increased by 0.31 eV compared with that in Pt/C-Si, indicating a strong EMSI between Pt NCs and CMK-3. The actual Pt content was quantitatively determined by ICP-OES (Table S2) and showed similar loading of Pt in Pt/CMK-3 (4.41 wt%) and Pt/C-Si (4.01 wt%). The content of  $\text{Pt}^{2+}$  in Pt/CMK-3 was 35.1%, while in Pt/C-Si was only 29.1%. This is due to the smaller size promoted better dispersion of Pt NCs on Pt/CMK-3 and led to a higher  $\text{Pt}^{2+}$  content, which is more conducive to the effective utilization of electrons in  $\text{Pt}^{2+}/\text{Pt}^0$  redox cycle. The high-resolution of O 1 s could be divided into two peaks at 532.2 eV and 533.4 eV (Fig. 1g), belonging to adsorbed oxygen ( $\text{O}_{\text{ads}}$ :  $\bullet\text{O}^2-$  and  $\bullet\text{OH}$  species) and surface residual water ( $\text{H}_2\text{O}_{\text{surf}}$ ). The presence of more reactive oxygen-containing groups on CMK-3 (Table S3) facilitates to reduce the energy barrier for activation of adsorbed O-oxygen species to generate ROSSs.

The reducibility and the amount of oxygen vacancies ( $O_v$ ) of Pt/CMK-3 and Pt/C-Si were measured by  $H_2$ -temperature-programmed reduction ( $H_2$ -TPR). There were three reduction peaks on Pt/CMK-3, and the two Gaussian-shape reduction peaks at 272 °C and 382 °C were the hydrogen consumption reduction peaks of  $Pt^{2+}$  to  $Pt^0$  species (Fig. S11a) [26]. Pt/CMK-3 displayed a lower temperature of the reduction peak (272 °C) than Pt/C-Si (367 °C), indicating that the coupling effect of EMSI and confinement effect significantly enhanced the metal reduction ability [27]. Generally, excellent low-temperature reducibility promotes the oxygen mobility and facilitates the adsorption-activation cycle of oxygen species [28]. Furthermore, cyclic voltammetry (CV) test was further used to analyze the redox ability of

catalysts (Fig. S11b). As is well known,  $O_3$  has a strong affinity for electrons and is easy to gain electrons to generate ROSS [4]. When  $O_3$  was saturated in the electrolyte solution, the oxidation peak located near 1.0 eV of Pt/CMK-3 and CMK-3 was significantly enhanced, indicating a strong electronic interaction between  $O_3$  and Pt NCs.

To further investigate the dispersibility, valence states and local atomic coordination structures of Pt NCs in Pt/C-Si and Pt/CMK-3, X-ray absorption near-edge structure (XANES) and extended X-ray fine structure (EXAFS) spectra were conducted. In Fig. 2a, the white line intensities of Pt/C-Si and Pt/CMK-3 were located between the comparison materials (Pt foil,  $PtCl_4$ ,  $PtO_2$ ), and the intensity of Pt/CMK-3 was slightly higher than that of Pt/C-Si, indicating that Pt in Pt/CMK-3 has a

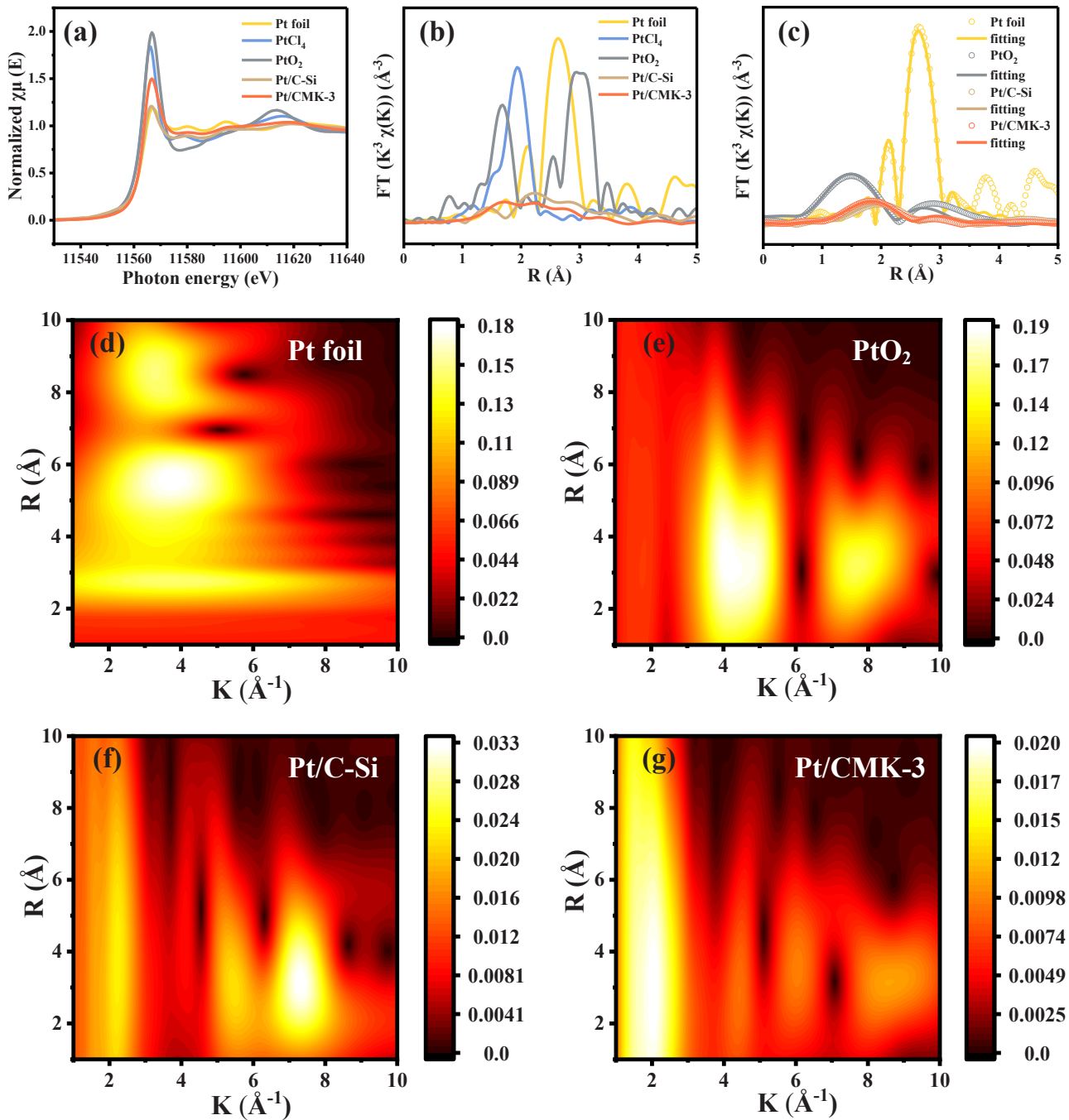


**Fig. 2.** (a) Pt L3-edge XANES spectra of Pt foil,  $PtCl_4$ ,  $PtO_2$ , Pt/C-Si and Pt/CMK-3; (b)  $k^3$ -weighted Pt L3-edge Fourier-transformed EXAFS spectra of Pt foil,  $PtCl_4$ ,  $PtO_2$ , Pt/C-Si and Pt/CMK-3; (c) Pt L3-edge EXAFS fitting results of Pt foil,  $PtO_2$ , Pt/C-Si and Pt/CMK-3 in R space; (d) - (g) Wavelet transforms of  $k^3$ -weighted EXAFS for Pt foil,  $PtO_2$ , Pt/C-Si and Pt/CMK-3.

higher oxidation state (such as  $\text{Pt}^{2+}$ ) and a lower coordination number compared with  $\text{PtO}_2$ , resulting in stronger interactions between Pt NCs and CMK-3 [29]. Fig. 2b displayed the R-space of Pt L3-edge in Pt/C-Si and Pt/CMK-3. The peak at 2.6 Å corresponded to Pt-Pt scattering, the peak at 1.6 Å was attributed to Pt-O bond and the peak at 1.95 Å was related to Pt-Cl bond [30]. The profiles of the weaker peak located around 1.5 Å (higher than Pt-O bond) in Pt/C-Si corresponded to Pt-C bond, indicating the interaction between Pt NCs and substrate through Pt-C coordination. It is noteworthy that a secondary peak can be also observed at 2.10 Å in both Pt/C-Si and Pt/CMK-3, but it does not exist in  $\text{PtO}_2$  and  $\text{PtCl}_4$ , implying a coupling effect between Pt-metal atoms except for Pt-C bonding. Moreover, the wavelet transforms (WT) analysis further confirmed the existence of Pt sites (Fig. 2d-g, Fig. S12). Compared with the control samples, the WT-EXAFS of Pt/C-Si and Pt/CMK-3 only displayed the main maximum intensity value between  $k \approx 2.0 \text{ \AA}^{-1}$  and  $R \approx 1.0\text{--}6.0 \text{ \AA}^{-1}$  were assigned to the Pt-C distance of the first neighbor shell. The higher WT intensity in Pt/CMK-3 suggested a stronger EMSI between Pt and CMK-3 [31]. The EXAFS fitting spectra of Pt foil,  $\text{PtO}_2$ , Pt/C-Si and Pt/CMK-3 were performed to probe quantitative atomic structure of Pt sites (Fig. 2c and Table S4). The coordination number of Pt was about 4.69 in Pt/C-Si, and the corresponding bond length was about  $2.00 \pm 0.08 \text{ \AA}$ . Whereas the coordination number of Pt in Pt/CMK-3 was about 1.81, and the corresponding bond length in R space was  $1.96 \pm 0.05 \text{ \AA}$ . The low-coordination structure facilitates the breaking of the centrosymmetric structure with higher electron cloud density metal centers and lower reaction energy barriers [32]. According to crystal field theory, the adsorption capacity between small molecules and catalyst is essentially a linear binding between the intermediate and the catalyst atomic orbitals [33]. Thus, the magnitude of the coordination number between Pt and C was closely related to the electron filling of d orbitals of Pt. The lower the coordination number of Pt in Pt/CMK-3, the more d electrons were filled in antibonding orbitals, thus effectively regulating the adsorption of the molecule. Whereas the higher  $\text{Pt}^{2+}$  content in Pt/CMK-3 also revealed a more suitable

adsorption capacity than Pt/C-Si, which is not too strong (with a higher  $\text{Pt}^0$  content) nor too weak (with a higher  $\text{Pt}^{2+}$  content).

### 3.2. Performance of $\text{CH}_3\text{SH}$ removal

In Fig. 3a,  $\text{CH}_3\text{SH}$  removal performance of C-Si and CMK-3 were 52.0% and 70.0%, and Pt/CMK-3 reached 97.0%, exceeding the state-of-the-art findings (Table S5). In contrast, the performance of Pt/C-Si first increased to 88.0% and gradually decreased to 80.0% after 1 h. This may be due to insufficient  $\text{Pt}^{2+}$  sites, making it difficult to adsorb  $\text{CH}_3\text{SH}$  [34]. Therefore, the relationship between the number of active sites (reflected by Pt loading) and the catalytic performance was further explored. When the theoretical loading of Pt NCs was 2.0 wt%, the removal efficiency was only 76.0%. In contrast, the performance was significantly enhanced to 97.0% when Pt NCs loading increased to 5.0 wt%. Notably, further increasing Pt loading to 10.0 wt%,  $\text{CH}_3\text{SH}$  removal efficiency decreased to 90.0% (Fig. 3b). This was attributed to the strong interactions between Pt atoms tend to induce the aggregation of Pt NCs to form nanoparticles (NPs) (Fig. S13a-f) according to Ostwald ripening theoretical [35,36]. The average size rapidly increases to 27.0 nm when Pt loading reached 10.0 wt% (Fig. S14a-b), and the  $\text{CH}_3\text{SH}$  transfer seems to be “blocked” by the large Pt NPs. Herein, three possible pathways for  $\text{CH}_3\text{SH}$  diffusion in Pt/CMK-3 may be proposed: (1) Fully free diffusion when Pt load is between 0 ~ 2.0 wt%; (2) Interfacial diffusion at Pt-C interface when Pt load reaches 5.0 wt%; and (3) Bulk phase diffusion when Pt load reaches 10.0 wt%. As mentioned above, the fully free diffusion of  $\text{CH}_3\text{SH}$  in CMK-3 or 2.0 wt% Pt/CMK-3 was very inefficient due to the weak interaction between  $\text{CH}_3\text{SH}$  and the catalyst, and the limited number of active sites for insufficient activation of  $\text{O}_3$  [37]. Similarly, as previously revealed in experiments, diffusion through the bulk phase of 10.0 wt% Pt/CMK-3 was difficult due to the large diffusion barrier. Therefore, the interfacial diffusion of  $\text{CH}_3\text{SH}$  in 5.0 wt% Pt/CMK-3 exhibits the highest efficiency and the optimal interaction capacity.

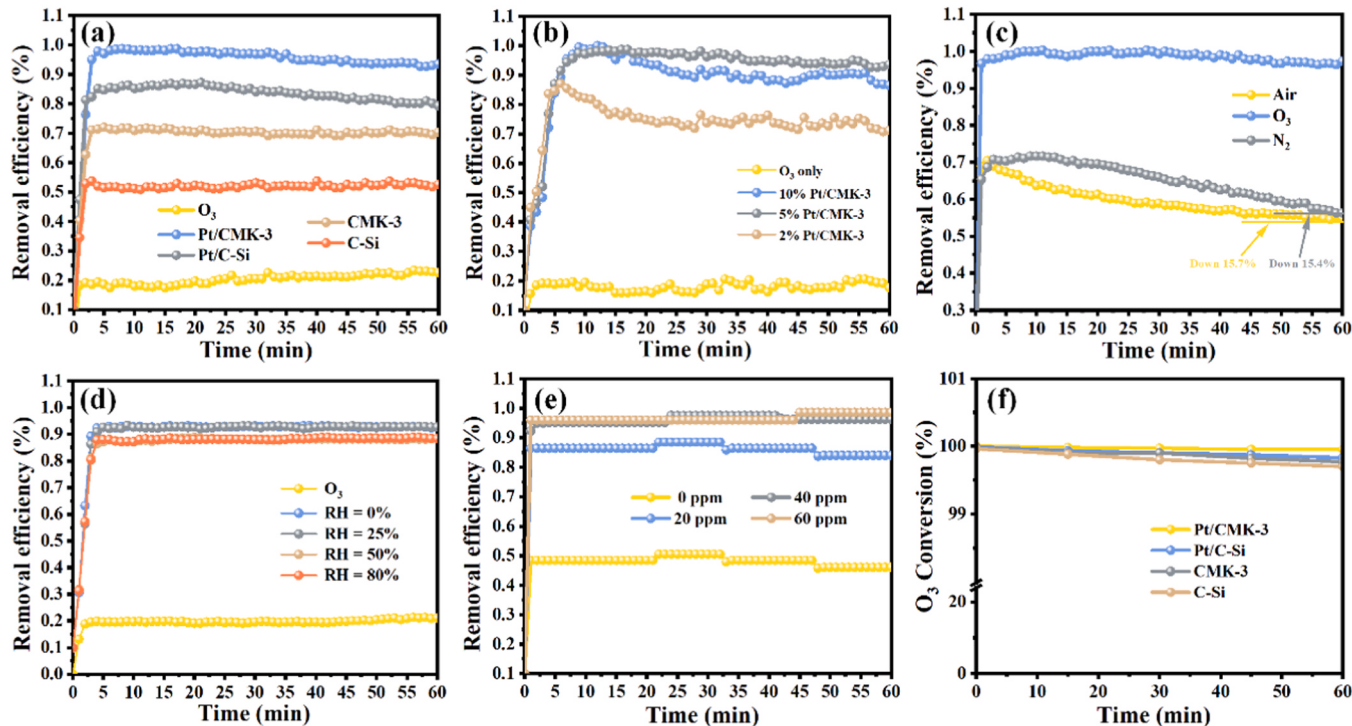


Fig. 3. (a) Catalytic ozonation for  $\text{CH}_3\text{SH}$  removal by Pt/CMK-3, Pt/C-Si, CMK-3, and C-Si; (b) Catalytic ozonation for  $\text{CH}_3\text{SH}$  removal by Pt/CMK-3 with different Pt loading; (c)  $\text{CH}_3\text{SH}$  removal under different atmospheres by Pt/CMK-3 and (d) Effect of humidity on catalytic ozonation for  $\text{CH}_3\text{SH}$  removal by Pt/CMK-3; (e) Effect of  $\text{O}_3$  concentration for  $\text{CH}_3\text{SH}$  removal by Pt/CMK-3; (f)  $\text{O}_3$  utilization efficiency in different systems. (Reaction conditions: [catalysts mass] = 30.0 mg,  $[\text{CH}_3\text{SH}]$  = 50 ppm,  $[\text{RH}]$  = 0%,  $[\text{O}_3]$  concentration = 40 ppm, [GHSV] = 200,000  $\text{mL h}^{-1} \text{g}^{-1}$ , and [temperature] = 25 °C.)

The ability of Pt/CMK-3 to activate  $O_3$  was further verified by the performance study of  $CH_3SH$  removal under different atmospheres. In Fig. 3c, Pt/CMK-3 displayed comparable removal efficiency about 62.0% under air and  $N_2$  atmospheres, but the removal efficiency decreased by 15.7% and 15.4% with the time prolonged to 1 h, respectively. The absence of oxidant ( $O_3$ ) in the air and  $N_2$  atmosphere may explain the challenge in generating ROSs within Pt/CMK-3 system, thereby impeding the efficient removal of  $CH_3SH$  and resulting in the accumulation of sulfur-containing intermediates on the catalyst. In contrast, the removal efficiency reached to 97.0% under  $O_3$  atmosphere. This result indicated that  $O_3$  efficiently activated by Pt/CMK-3 and generated large amounts of ROSs through chain reactions. Relative humidity (RH) also has great influence on the catalytic performance in gas-solid catalytic system. The performance of  $CH_3SH$  removal kept around 93.0% when RH was 0%, 25%, and 50% (Fig. 3d), which indicated that the presence of moderate amount of  $H_2O$  molecules in the system was beneficial to the formation of intermediates oxidation species ( $^*OH/^*O$ ), further improved the catalytic performance. When RH increased to 80%, the performance slightly decreased (88.0%), indicating that Pt/CMK-3 has better resistance to moisture [13]. In addition, the effect of  $O_3$  concentration on the catalytic activity was further explored. When the  $O_3$  concentration was 0 ppm, the removal efficiency of  $CH_3SH$  was about 52.0%. With the increase of  $O_3$  concentration, the removal efficiency increased significantly and reached 99.5% when the  $O_3$  concentration was 60 ppm (Fig. 3e). These results further demonstrated the important role of  $O_3$  as an oxidant in the removal of  $CH_3SH$ . The  $O_3$  concentration at the reactor outlet was monitored to assess the efficiency of  $O_3$  utilization. Fig. 3f illustrated that the  $O_3$  conversion rate of Pt/CMK-3 system was 99.95%, better than other systems. The residual  $O_3$  concentration at the outlet of reactor was below 0.02 ppm, indicating that the high efficiency of  $O_3$  utilization in the catalytic ozonation process by Pt/CMK-3, so as to avoid secondary pollution by the elevated  $O_3$  levels in the exhaust gas.

Furthermore, the performance of  $CH_3SH$  removal in confined Pt/

CMK-3 system remained at a satisfactory level (89.5%) after 8 cycles (Fig. S15a). In addition, XRD patterns further proved the structure did not change after long-term reaction. TEM images also revealed no obvious aggregation of Pt NCs, and the size was consistent with the initial state (Fig. S15b-d). These results indicated that CMK-3 can better stabilize Pt NCs, thus ensuring a good physical structure stability and catalytic activity of Pt/CMK-3.

### 3.3. Analysis of intermediate products

In situ diffuse reflectance infrared Fourier transform spectroscopy (in-situ DRIFTS) was employed to determine the possible intermediate products. In Fig. 4a, the strong bands observed near  $2950\text{ cm}^{-1}$ ,  $950\text{ cm}^{-1}$ , and  $810\text{ cm}^{-1}$  corresponded to the stretching vibration of C-H bond, vibration of S-C-H bond, and vibration of C-H bond [38], respectively. The appearance of absorption peaks indicated that  $CH_3SH$  was adsorbed on Pt/CMK-3 and partially undergoes conversion to form primary product. Noteworthy, the weaker bands at  $1256\text{ cm}^{-1}$  and  $1078\text{ cm}^{-1}$  could be attributed to the R-SO<sub>2</sub>-R vibration and S=O vibration of SO<sub>3</sub><sup>2-</sup> [39], which also indicated that some of the adsorbed  $CH_3S^-$  was further oxidized to intermediate products or C-S bond broken to formed SO<sub>3</sub><sup>2-</sup> during the adsorption process. For HCO process (Fig. 4b), the signals of the bands related to oxidation products became stronger, indicating that Pt/CMK-3 more completely oxidized  $CH_3SH$ . In detail, the characteristic bands of  $CH_3SH$  in the adsorption phase significantly weakened or even disappeared, indicating that the  $CH_3S^-$  further oxidized to other products with the involvement of  $O_3$ . And the bands associated with ozonated substances ( $O_3$ ) at  $780\text{ cm}^{-1}$  and SO<sub>4</sub><sup>2-</sup> vibrations at  $1052\text{ cm}^{-1}$  increased with time going on [40]. In contrast, a series of new bands at  $1715\text{ cm}^{-1}$ ,  $1591\text{ cm}^{-1}$  were assigned to C=O stretching vibrations of -COO and  $\nu(COO^-)$  peaks of HCOOH [41], while the bands at  $1379\text{ cm}^{-1}$ ,  $1204\text{ cm}^{-1}$  were associated with sulfonate CH<sub>3</sub>SO<sub>3</sub><sup>-</sup> vibrations [42]. The important intermediate species were normalized in adsorption process, and the intensity of chemisorbed

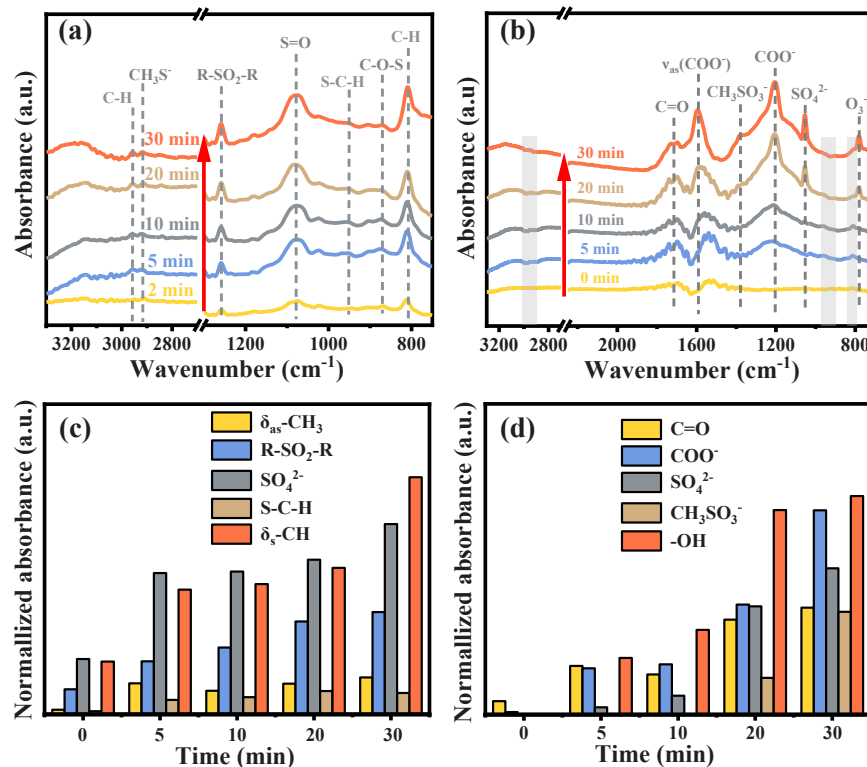


Fig. 4. In-situ DRIFTS spectra of  $CH_3SH$  adsorption (a) and catalytic ozonation (b) over Pt/CMK-3; Normalized species evolution of (c)  $CH_3SH$  adsorption and (d) catalytic ozonation over Pt/CMK-3.

$\text{CH}_3\text{SH}$  and  $\text{SO}_4^{2-}$  grew with adsorption time (Fig. 4c), while the bands of S-C-H and -CH<sub>3</sub> ( $\text{CH}_3\text{SSCH}_3$ ,  $\text{CH}_3\text{SCH}_3$ ) stabilize around 20 min, indicating that  $\text{CH}_3\text{SSCH}_3$  and  $\text{CH}_3\text{SCH}_3$  were the main intermediate products of the adsorption process. In addition,  $\text{CH}_3\text{SH}$  was gradually oxidized during the HCO process (Fig. 4d), the intensity of  $\text{CH}_3\text{SO}_3$  and  $\text{SO}_4^{2-}$  intermediates bands increased, while the intensity of the -COO and -OH like product bands fluctuated during the reaction, which was attributed to the final oxidation of  $\text{HCOOH}$  and  $\text{C=O}$  to form harmless  $\text{CO}_2$  and further escape from Pt/CMK-3. Furthermore, the difference in hydrophobicity between Pt/C-Si and Pt/CMK-3 (Fig. S16) also confirmed the enhanced mass transfer of Pt/CMK-3 to generate more ROSSs. The exhaust gas products were determined and analyzed by PTR-TOF-MS, the mass spectra displayed in Fig. S17 and Table S6. Compared with Pt/C-Si system (Fig. S17a), the signal of  $\text{CH}_3\text{SH}$  ( $m/z=49.01$ ) in the exhaust gas during catalytic ozonation by Pt/CMK-3 was weaker (Fig. S17b). Furthermore, the signals of intermediate products such as  $\text{CH}_3\text{CHO}$  ( $m/z=45.03$ ) and  $\text{CH}_3\text{SOH}$  ( $m/z=65.00$ ) in Pt/CMK-3 system were relatively weak, suggesting that the degradation of  $\text{CH}_3\text{SH}$  involves the cleavage of C-S and C-H bonds. This result indicated that Pt/CMK-3 system displayed a more efficient  $\text{CH}_3\text{SH}$  removal, and the final products in outlet were mainly inorganic mineralized  $\text{CO}_2$  and  $\text{SO}_4^{2-}$ .

The oxidation products were further analyzed to compare the activity of Pt/CMK-3 and Pt/C-Si systems (Fig. S18). Initially, the  $\text{CO}_2$  production in the exhaust gas was assessed and it was shown that  $\text{CO}_2$  content in Pt/CMK-3 system was  $2.15 \times 10^{-5}$  mmol, while minimum  $\text{CO}_2$  production in Pt/C-Si system was  $5.60 \times 10^{-6}$  mmol. Furthermore, the presence of  $\text{SO}_4^{2-}$  on the catalyst surface was confirmed using IC. After 1 h of reaction, the content of  $\text{SO}_4^{2-}$  on Pt/CMK-3 surface was  $4.39 \times 10^{-5}$  mmol, significantly higher than that of Pt/C-S system ( $6.56 \times 10^{-6}$  mmol), indicating that Pt/CMK-3 system has good oxidation and mineralization of  $\text{CH}_3\text{SH}$  and finally convert it into  $\text{CO}_2$  and  $\text{SO}_4^{2-}$ .

### 3.4. Investigation of reactive oxygen species (ROSS)

Electron paramagnetic resonance (EPR) experiment was used to ascertain the ROSSs generated in HCO process. In Fig. 5a, Pt/CMK-3 detected a clear 1:2:2:1 quadruplet signal of DMPO-•OH [43] and showed higher intensity than that in Pt/C-Si system and sole  $\text{O}_3$  condition, indicating that Pt/CMK-3 more easily activating  $\text{O}_3$  to generate •OH. In addition, DMPO-•OH gradually increased with the prolonged exposure time to 10 min (Fig. 5d), indicating that •OH was the main ROSSs in removal of  $\text{CH}_3\text{SH}$  in Pt/CMK-3 system. The significant signal peaks of DMPO-• $\text{O}_2^-$  (1:1:1:1) [44] was observed in confined Pt/CMK-3 system (Fig. 5b), and its signal intensities of • $\text{O}_2^-$  radicals were further enhanced with the time extended to 10 min of introduce  $\text{O}_3$  in confined Pt/CMK-3 system (Fig. 5e), indicating that  $\text{O}_3$  was continuously activated to generate • $\text{O}_2^-$  as the main ROS in HCO process. The characteristic signals of TEMP- $^1\text{O}_2$  were shown in Fig. 5c and Pt/CMK-3 system had the strongest triple 1:1:1 typical signals [10], while the typical signals gradually increased with time prolonged to 10 min in confined Pt/CMK-3 system (Fig. 5f), which meant the large number of  $^1\text{O}_2$  was generated. In-situ Raman used to further explore the activation of  $\text{O}_3$ . Except for the original D and G bands of Pt/CMK-3 system, three new characteristic peaks were observed at 850, 1020 and 1090  $\text{cm}^{-1}$  (Fig. S19a, b), corresponding to the adsorbed peroxide species ( $^* \text{O}_2$ ), adsorbed atomic oxygen ( $^* \text{O}_{\text{ads}}$ ) and surface- $\text{O}_3$  [45], respectively. In contrast, under  $\text{N}_2$  atmosphere, no significant signal peaks of oxidatively active species were detected in Pt/CMK-3 (Fig. S19c, d), indicating that  $\text{O}_3$  was the main electron acceptor and the initial species of free radical chain reaction [46]. From these results, we found that  $\text{Pt}^0$  can activated  $\text{O}_3$  to  $^* \text{O}_2$  and  $^* \text{O}_{\text{ads}}$  in the confined Pt/CMK-3 system, and  $^* \text{O}_{\text{ads}}$  (ORP = 2.43 V) and  $^* \text{O}_2$  (ORP = 1.35 V) [4] with a certain oxidation capacity can partial oxidation  $\text{CH}_3\text{SH}$  to intermediate products.

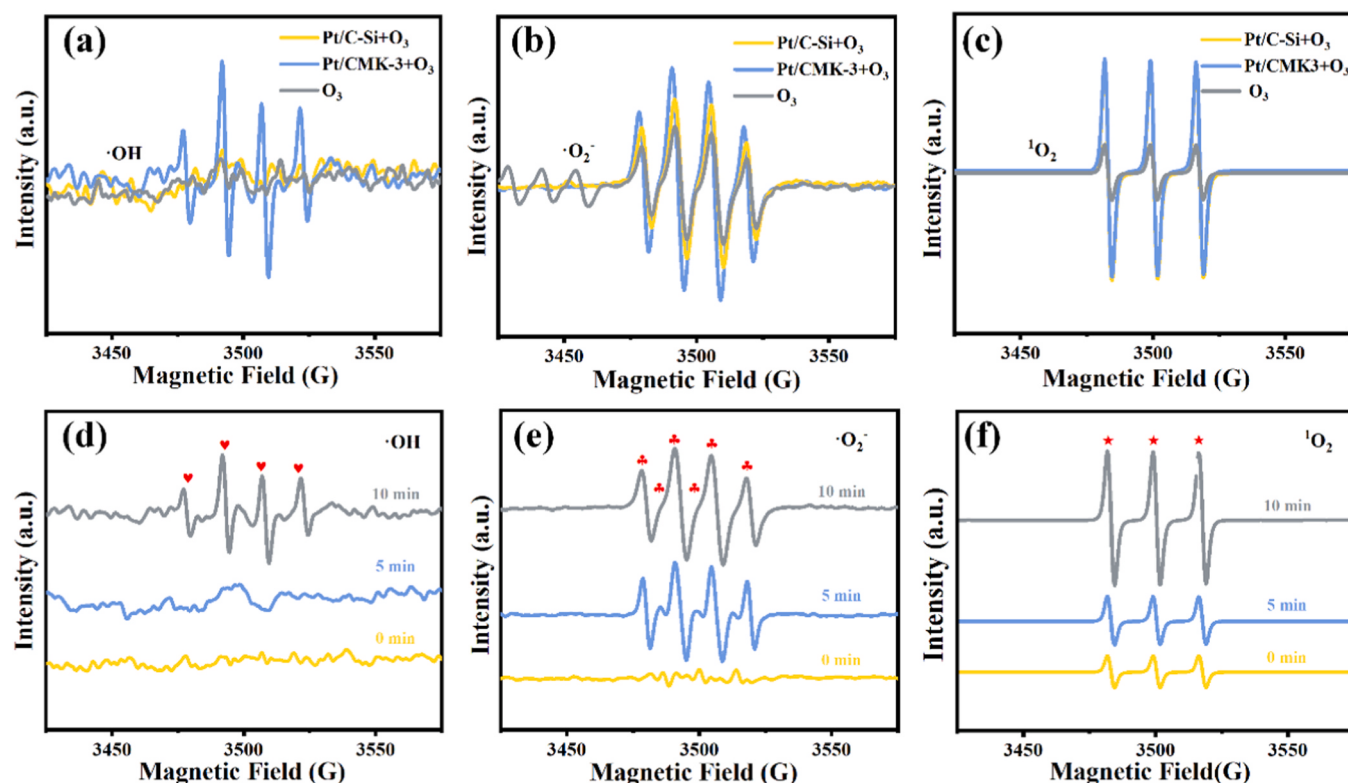


Fig. 5. EPR spectra of (a) DMPO-•OH, (b) TEMP-• $\text{O}_2^-$  and (c) DMPO- $^1\text{O}_2$  in different systems; EPR spectra of (d) DMPO-•OH, (e) TEMP-• $\text{O}_2^-$  and (f) DMPO- $^1\text{O}_2$  for catalytic ozonation with Pt/CMK-3 system of different reaction time.

### 3.5. Reaction Mechanism

The valence states of Pt and relative content situation before and after reactions were explored to further investigative the reaction mechanism (Fig. S20a, b and Table S7). After catalytic reaction, the content of  $\text{Pt}^0$  on Pt/CMK-3 slightly decreased from 64.9% to 60.7%, and the content of  $\text{Pt}^{2+}$  content slightly increased from 35.1% to 39.3%. The result demonstrated that the electron-rich region of  $\text{Pt}^0$  in Pt/CMK-3 transfers electrons to  $\text{O}_3$  to generate intermediate oxygen species ( $^*\text{O}_2$  and  $^*\text{O}_{\text{ads}}$ ), while the contaminants can act as electron donors to adsorb at the electron-deficient center of the catalyst to maintain the electron gain/loss balance of the catalyst [47]. In addition, after  $\text{CH}_3\text{SH}$  was adsorbed on Pt/CMK-3, the content of  $\text{Pt}^0$  increased from 64.9% to 70.2%, indicating that electrons were transferred from  $\text{CH}_3\text{SH}$  to  $\text{Pt}^{2+}$ , and  $\text{CH}_3\text{SH}$  lost electrons to become  $\text{CH}_3\text{S}\bullet/\text{CH}_3\text{SSCH}_3$ . The catalytic performance was maintained through the electron cycle between Pt,  $\text{O}_3$  and  $\text{CH}_3\text{SH}$ , and as well as the continuous activation of  $\text{O}_3$  by  $\text{Pt}^0$ . In contrast, the content of  $\text{Pt}^0$  on Pt/C-Si decreased more significantly from

70.9% to 60.6% after reaction, while the  $\text{Pt}^{2+}$  content increased from 29.1% to 39.4%, which may be ascribed to that partial  $\text{Pt}^0$  (loaded outside of C-Si) was easily oxidized to  $\text{Pt}^{2+}$  by excess  $\text{H}_2\text{O}$  and  $\text{O}_2$ , and thus the catalytic performance decreased as the reaction proceeded.

DFT calculations were carried out to reveal the catalytic mechanism on molecular level. Subsequently, the theoretical structure model was built and optimized (Fig. S21a, b), the formation energy of Pt/CMK-3 was  $-5.40$  eV, while Pt/C-Si was  $-2.92$  eV. The lower formation energy meant Pt/CMK-3 had better structural stability [48]. Besides, the adsorption energy ( $E_{\text{ads}}$ ) of  $\text{O}_3$  and  $\text{CH}_3\text{SH}$  on Pt/CMK-3 and Pt/C-Si (Fig. 6a, b) revealed that the binding strength of  $\text{O}_3$  to Pt/CMK-3 ( $E_{\text{ads}} = -3.45$  eV) was higher than that of Pt/C-Si ( $E_{\text{ads}} = -2.09$  eV). The corresponding bond length of  $\text{O}_1\text{-O}_2$  stretched from  $1.29$  Å to  $1.94$  Å (Table S8), indicating that  $\text{Pt}^0$  sites can directly enhanced adsorption/activation of  $\text{O}_3$  and facilitates the generation of  $^*\text{O}_{\text{ads}}$  and  $^*\text{O}_2$ . In contrast, the  $\text{O}_1\text{-O}_2$  bond length was only stretched from  $1.29$  Å to  $1.81$  Å, indicating that Pt/C-Si has little ability to adsorb and activate  $\text{O}_3$ . Since both  $\text{O}_3$  and  $\text{CH}_3\text{SH}$  molecules are present in the system, the

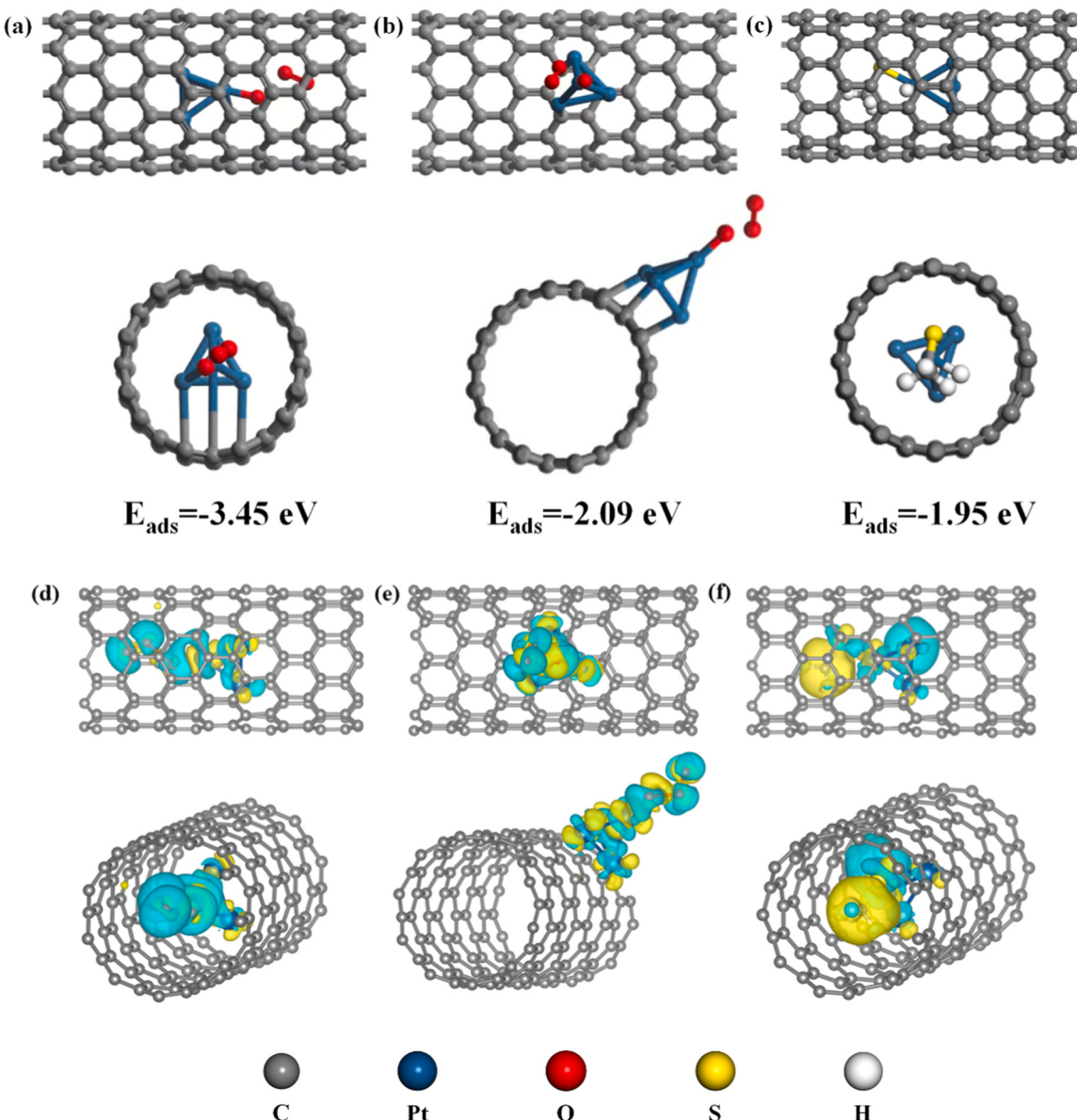


**Fig. 6.** Adsorption energy of  $\text{O}_3$  on (a) Pt/CMK-3 and (b) Pt/C-Si; (c) Adsorption energy of  $\text{CH}_3\text{SH}$  on Pt/CMK-3; Charge density difference (CDD) of (d) Pt/CMK-3, (e) Pt/C-Si after adsorption of  $\text{O}_3$  and (f) Charge density difference (CDD) of Pt/CMK-3 adsorption of  $\text{CH}_3\text{SH}$  (Blue region indicates electron accumulation, yellow region indicates electron depletion).

adsorption order and adsorption strength in confined Pt/CMK-3 system need to be further investigated. In Fig. 6c,  $E_{ads}$  of  $\text{CH}_3\text{SH}$  on  $\text{Pt}^{2+}$  sites of Pt/CMK-3 (-1.95 eV) was smaller than that of  $\text{O}_3$  on  $\text{Pt}^0$  sites of Pt/CMK-3 (-3.45 eV), implying a highly exothermic adsorption process, and meant that  $\text{O}_3$  has stronger adsorption ability on Pt/CMK-3, and accept electrons from  $\text{Pt}^0$  to generate large number of ROS due to strong electronic interactions. However, the electron interaction between  $\text{CH}_3\text{SH}$  and  $\text{Pt}^{2+}$  is weaker, tending to donate electrons to generate  $\text{CH}_3\text{S}\bullet/\text{CH}_3\text{SSCH}_3$ , ultimately maintaining the redox cycle of  $\text{Pt}^0/\text{Pt}^{2+}$  [49]. The d-band center (ed) was used to semi-quantitatively describe the adsorption strength of  $\text{CH}_3\text{SH}$  (Fig. S22). And ed position of Pt decreased from -1.74 eV to -2.10 eV after  $\text{CH}_3\text{SH}$  adsorbed on Pt/CMK-3, which was lower than the change of Pt/C-Si (-1.75 eV to -1.83 eV), this attributed to the d-orbitals of  $\text{Pt}^{2+}$  gained electrons from  $\text{CH}_3\text{SH}$ , resulting in the further weakening of the binding strength of the  $\text{CH}_3\text{SH}$  molecule. Considering the too strong binding on  $\text{Pt}^{2+}$  for oxidation, the weaker adsorption energy of Pt/CMK-3 is essential for an enhanced  $\text{CH}_3\text{SH}$  removal efficiency [50]. Charge density difference (CDD) of  $\text{O}_3+\text{Pt/CMK-3}$  (Fig. 6d) and  $\text{O}_3+\text{Pt/C-Si}$  (Fig. 6e) illustrated the O atoms in  $\text{O}_3$  strongly gain electrons from  $\text{Pt}^0$  in Pt/CMK-3 [51]. However, the CDD between  $\text{O}_3$  and Pt NCs was more heterogeneous in Pt/C-Si system, indicating a weaker electronic interaction between  $\text{O}_3$  and Pt/C-Si. The CDD of  $\text{CH}_3\text{SH-Pt/CMK-3}$  (Fig. 6f) and Bader charge analysis (Fig. S23) illustrated that C and S atoms in  $\text{CH}_3\text{SH}$  lost about 0.25 |e| and 0.08 |e|, the average Pt NCs gained about 0.05 |e|, respectively.

The electrostatic potential results presented the electron distribution of  $\text{CH}_3\text{SH}$  molecule was prone to rearrangement due to the electronegativity difference between the C and S elements, and it was easy to

$\text{O}_3$  and  $\text{CH}_3\text{SH}$  in different systems, compared with  $\text{O}_3+\text{Pt/CMK-3}$  ( $\text{MSD} = 7.22 \times 10^{-15} \text{ m}^2 \text{ s}^{-1}$ ), the average displacement of  $\text{O}_3$  is smaller in  $(\text{O}_3+\text{CH}_3\text{SH})+\text{Pt/CMK-3}$  system ( $\text{MSD} = 2.76 \times 10^{-15} \text{ m}^2 \text{ s}^{-1}$ ). In addition, the diffusion coefficients ( $D_c$ ) of  $\text{O}_3$  and  $\text{CH}_3\text{SH}$  in confined Pt/CMK-3 system were calculated based on MSD of 1 ns [55]. In Fig. 7d, the  $D_c$  of  $\text{O}_3$  ( $0.0046 \text{ nm}^2 \text{ ps}^{-1}$ ) was lower than that of  $\text{CH}_3\text{SH}$  ( $0.022 \text{ nm}^2 \text{ ps}^{-1}$ ), which revealed the physical interaction (collision, repulsion, etc.) exists between  $\text{O}_3$  and  $\text{CH}_3\text{SH}$  during the diffusion process, this meant that the mass transfer process will be more sequential, and further reduce the energy loss in the mass transfer process and increase the efficiency of mass transfer [56].

Based on ex/in-situ experiments and theoretical calculations, the process of  $\text{CH}_3\text{SH}$  removal in confined Pt/CMK-3 system can be divided into two processes: during adsorption process, the interfacial diffusion triggered by the confinement effect of Pt/CMK-3 significantly enhances the effective mass transfer of  $\text{O}_3$  and  $\text{CH}_3\text{SH}$ . This allows  $\text{CH}_3\text{SH}$  and  $\text{O}_3$  to diffuse synchronized to the  $\text{Pt}^{2+}$  sites and  $\text{Pt}^0$  sites, and undergo electronic interactions that promote more electron delocalization. The strong chemisorption and electron transfer processes for the d-p orbital hybridization between Pt NCs and  $\text{CH}_3\text{SH}$  oxidized  $\text{CH}_3\text{SH}$  to  $\text{CH}_3\text{S}\bullet/\text{CH}_3\text{S}^\bullet$ , and further break C-S bond to formed  $\text{CH}_3\text{CHO}$ ,  $\text{CH}_3\text{SOCH}_3$ ,  $\text{SO}_3^{2-}$  intermediates; In catalytic ozonation process, the absorbed  $\text{O}_3$  in  $\text{Pt}^0$  sites was activated to generate oxygenated intermediates ( ${}^*\text{O}_{ads}$  and  ${}^*\text{O}_2$ ), further transformed into other strong oxidation ROSs ( $\bullet\text{OH}$ ,  ${}^*\text{O}_2$ ,  ${}^1\text{O}_2$ ) and deeply oxidized primary products to  $\text{SO}_4^{2-}$ ,  $\text{CO}_2$  and  $\text{H}_2\text{O}$ .

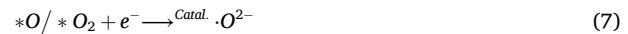
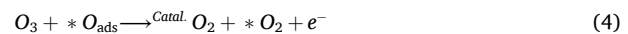
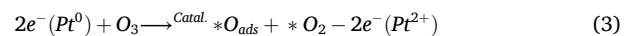
The summarized reaction pathways following:

(1) Adsorption stage

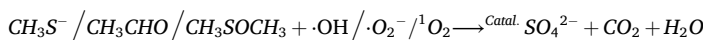
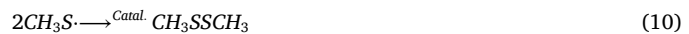
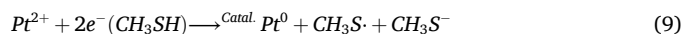


(2)

(2) The chain reaction of ROS: (\* refers to the active site on the catalyst)



(3)  $\text{CH}_3\text{SH}$  catalytic ozonation stage:



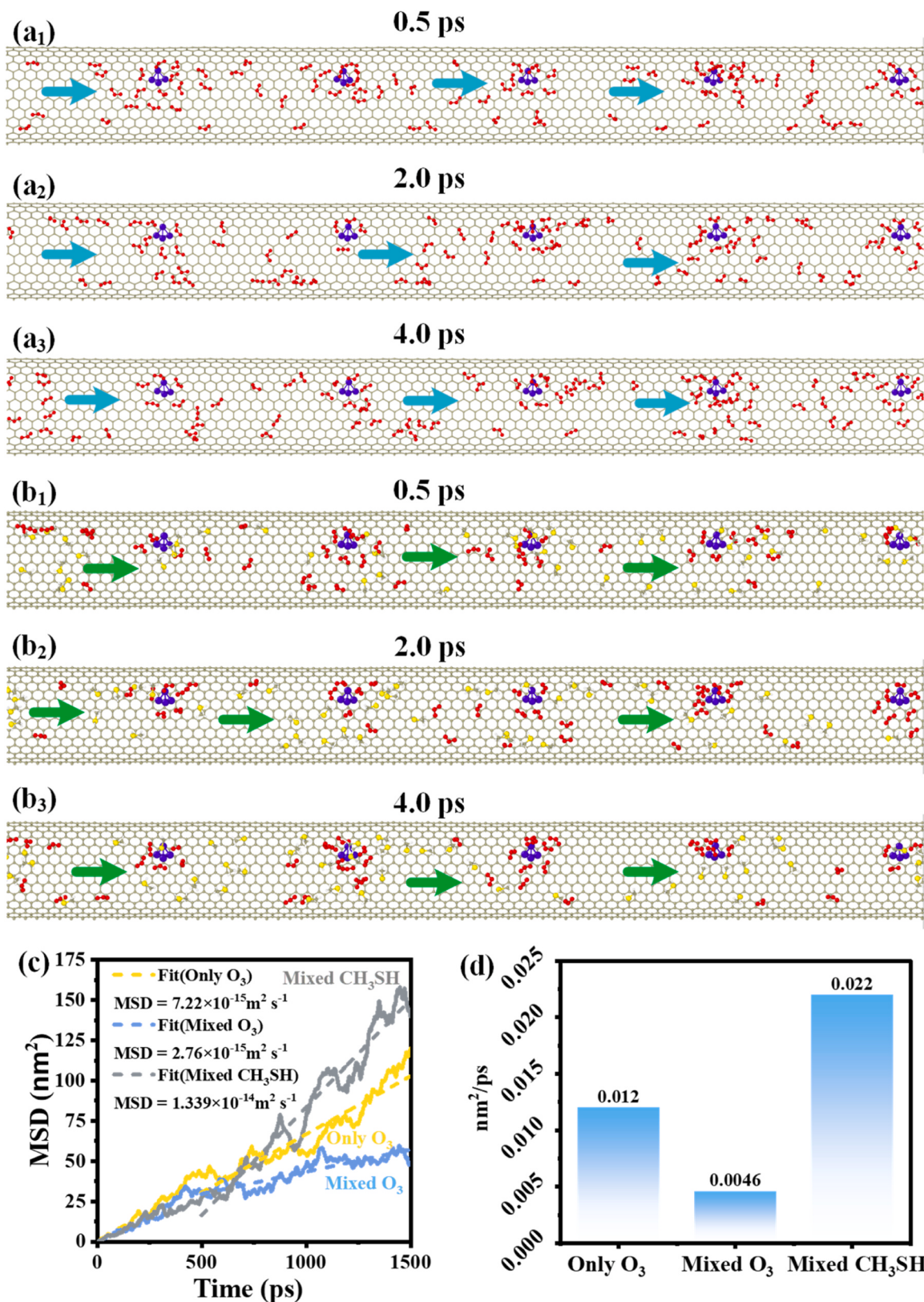


**Fig. 7.** Typical snapshots of dynamic diffusion changes of O<sub>3</sub> alone at 0.5, 2.0, 4.0 ps (a<sub>1</sub>, a<sub>2</sub>, a<sub>3</sub>) and O<sub>3</sub>+CH<sub>3</sub>SH on Pt/CMK-3 at 0.5, 2.0, 4.0 ps (b<sub>1</sub>, b<sub>2</sub>, b<sub>3</sub>); The corresponding (c) mean square displacement (MSD) and (d) diffusion coefficients (Dc) of O<sub>3</sub> and CH<sub>3</sub>SH vs. AIMD simulation time.

#### 4. Conclusions

This study emphasizes an innovative strategy to effectively remove CH<sub>3</sub>SH through local microenvironment modulation of Pt<sup>0</sup>/Pt<sup>2+</sup> NCs inducing synchronous mass transfer. The rational confined structure of catalysts can effectively enhance the mass transfer efficiency of gaseous oxidant molecules (O<sub>3</sub>) and gaseous pollutant molecules (CH<sub>3</sub>SH). The effective interfacial diffusion of O<sub>3</sub> and CH<sub>3</sub>SH at Pt-C interface with appropriate metal loading (5.0% Pt/CMK-3) through synchronous mass transfer, enables O<sub>3</sub> and CH<sub>3</sub>SH transfer to Pt<sup>0</sup> and Pt<sup>2+</sup> sites in the confined Pt/CMK-3 system, respectively, thus leading to the significantly increased removal of CH<sub>3</sub>SH. In addition, DFT calculations and AIMD analysis further elucidate the intrinsic mechanism of O<sub>3</sub> activation and CH<sub>3</sub>SH elimination. In summary, the study not only opens a new avenue for in-depth investigation on the diffusion mechanisms and kinetic properties of gaseous reaction between oxidant molecules and pollutant molecules at the catalyst surface/interface, but also provides new ideas for rational design of catalyst structure.

#### CRediT authorship contribution statement

**Tao Zhong:** Methodology, Validation, Computation, Investigation, Data curation, Writing – original draft, Visualization. **Xianhu Long:** Data curation, Visualization. **Manhui Luo:** Data curation, Visualization. **Su Tang:** Data curation, Formal analysis. **Wenbin Huang:** Data curation, Formal analysis. **Huinan Zhao:** Writing – review & editing, Methodology, Validation, Investigation, Data curation, Software. **Lingling Hu:** Writing – review & editing, Methodology, Validation, Investigation, Data curation, Software. **Shuanghong Tian:** Conceptualization, Supervision, Funding acquisition, Writing – review & editing. **Dong Shu:** Conceptualization, Supervision, Funding acquisition, Writing – review & editing. **Chun He:** Conceptualization, Supervision, Funding acquisition, Writing – review & editing.

#### Declaration of Competing Interest

The authors declare that they have no known competing financial interests or personal relationships that could have appeared to influence the work reported in this paper.

#### Data availability

Data will be made available on request.

#### Acknowledgements

The authors thank the National Natural Science Foundation of China (No. 52070195, 21876212, 21673086), Guangdong Basic and Applied Basic Research Foundation (No. 2023A1515012198) for financially supporting this work.

#### Appendix A. Supporting information

Supplementary data associated with this article can be found in the online version at [doi:10.1016/j.apcatb.2024.124162](https://doi.org/10.1016/j.apcatb.2024.124162).

#### References

- C. Li, P.G. Choi, Y. Masuda, Highly sensitive and selective gas sensors based on NiO/MnO<sub>2</sub>@NiO nanosheets to detect allyl mercaptan gas released by humans under psychological stress, *Adv. Sci.* 9 (2022) 2202442, <https://doi.org/10.1002/advs.202202442>.
- T. Huang, Q. Peng, W. Shi, J. Xu, Y. Fan, An anionic surfactant-assisted equilibrium adsorption method to prepare highly dispersed Fe-promoted Ni/Al<sub>2</sub>O<sub>3</sub> catalysts for highly selective mercaptan removal, *Appl. Catal. B: Environ.* 230 (2018) 154–164, <https://doi.org/10.1016/j.apcatb.2018.02.053>.
- S. Zhao, D. Kang, Y. Liu, Y. Wen, X. Xie, H. Yi, X. Tang, Spontaneous Formation of Asymmetric Oxygen Vacancies in Transition-Metal-Doped CeO<sub>2</sub> Nanorods with Improved Activity for Carbonyl Sulfide Hydrolysis, *ACS Catal.* 10 (2020) 11739–11750, <https://doi.org/10.1021/acscatal.0c02832>.
- Y. Huang, D. Ma, W. Liu, D. Xia, L. Hu, J. Yang, P. Liao, C. He, Enhanced catalytic ozonation for eliminating CH<sub>3</sub>SH via graphene-supported positively charged atomic pt undergoing Pt<sup>2+</sup>/Pt<sup>4+</sup> Redox Cycle, *Environ. Sci. Technol.* 55 (2021) 16723–16734, <https://doi.org/10.1021/acs.est.1c06938>.
- W. Qu, M. Luo, Z. Tang, T. Zhong, H. Zhao, L. Hu, D. Xia, S. Tian, D. Shu, C. He, Accelerated catalytic ozonation in a mesoporous carbon-supported atomic Fe-N4 sites nanoreactor: confinement effect and resistance to poisoning, *Environ. Sci. Technol.* 57 (2023) 13205–13216, <https://doi.org/10.1021/acs.est.2c08101>.
- W. Qu, Z. Tang, H. Wen, M. Luo, T. Zhong, Q. Lian, L. Hu, S. Tian, C. He, D. Shu, Electron transfer trade-offs in MOF-derived cobalt-embedded nitrogen-doped carbon nanotubes boost catalytic ozonation for gaseous sulfur-containing VOC elimination, *ACS Catal.* 13 (2023) 692–705, <https://doi.org/10.1021/acscatal.2c05285>.
- G. Zhu, W. Zhu, Y. Lou, J. Ma, W. Yao, R. Zong, Y. Zhu, Encapsulate  $\alpha$ -MnO<sub>2</sub> nanofiber within graphene layer to tune surface electronic structure for efficient ozone decomposition, *Nat. Commun.* 12 (2021) 4152, <https://doi.org/10.1038/s41467-021-24424-x>.
- W. Ye, X. Li, B. Zhang, W. Liu, Y. Cheng, X. Fan, H. Zhang, Y. Liu, Q. Dong, M.-S. Wang, Superfast Mass Transport of Na/K Via mesochannels for dendrite-free metal batteries, *Adv. Mater.* 35 (2023) 2210447, <https://doi.org/10.1002/adma.202210447>.
- Z. Wang, K. Li, J. Guo, H. Liu, Y. Zhang, P. Dang, J. Wang, Enhanced mass transfer of ozone and emerging pollutants through a gas-solid-liquid reaction interface for efficient water decontamination, *Environ. Sci. Technol.* (2023), <https://doi.org/10.1021/acs.est.2c07688>.
- Z. Yang, J. Qian, A. Yu, B. Pan, Singlet oxygen mediated iron-based Fenton-like catalysis under nanoconfinement, *Proc. Natl. Acad. Sci.* 116 (2019) 6659–6664, <https://doi.org/10.1073/pnas.1819382116>.
- D. Guo, Y. Yao, S. You, L. Jin, P. Lu, Y. Liu, Ultrafast degradation of micropollutants in water via electro-periodate activation catalyzed by nanoconfined Fe<sub>2</sub>O<sub>3</sub>, *Appl. Catal. B: Environ.* 309 (2022) 121289, <https://doi.org/10.1016/j.apcatb.2022.121289>.
- J. Chen, Y. Ha, R. Wang, Y. Liu, H. Xu, B. Shang, R. Wu, H. Pan, Inner Co synergizing outer ru supported on carbon nanotubes for efficient pH-universal hydrogen evolution catalysis, *Nano-Micro Lett.* 14 (2022) 186, <https://doi.org/10.1007/s40820-022-00933-2>.
- W. Dai, B. Zhang, J. Ji, B. Liu, R. Xie, Y. Gan, X. Xie, J. Zhang, P. Huang, H. Huang, Exceptional Ozone Decomposition over  $\delta$ -MnO<sub>2</sub>/AC under an Entire Humidity Environment, *Environ. Sci. Technol.* (2023), <https://doi.org/10.1021/acs.est.3c00717>.
- J. Wu, J. Wang, C. Liu, C. Nie, T. Wang, X. Xie, J. Cao, J. Zhou, H. Huang, D. Li, S. Wang, Z. Ao, Removal of gaseous volatile organic compounds by a multiwalled carbon nanotubes/peroxymonosulfate wet scrubber, *Environ. Sci. Technol.* 56 (2022) 13996–14007, <https://doi.org/10.1021/acs.est.2c03590>.
- B. Liu, W. Song, H. Wu, Z. Liu, Y. Teng, Y. Sun, Y. Xu, H. Zheng, Degradation of norfloxacin with peroxymonosulfate activated by nanoconfinement Co<sub>3</sub>O<sub>4</sub>@CNT nanocomposite, *Chem. Eng. J.* 398 (2020) 125498, <https://doi.org/10.1016/j.cej.2020.125498>.
- Z.-W. Wei, H.-J. Wang, C. Zhang, K. Xu, X.-L. Lu, T.-B. Lu, Reversed charge transfer and enhanced hydrogen spillover in platinum nanoclusters anchored on titanium oxide with rich oxygen vacancies boost hydrogen evolution reaction, *Angew. Chem. Int. Ed.* 60 (2021) 16622–16627, <https://doi.org/10.1002/anie.202104856>.
- L. Zhang, Z. Zhu, W. Tan, J. Ji, Y. Cai, Q. Tong, Y. Xiong, H. Wan, L. Dong, Thermal-driven optimization of the strong metal-support interaction of a platinum-manganese oxide octahedral molecular sieve to promote toluene oxidation: effect of the interface Pt<sup>2+</sup>-O<sub>v</sub>-Mn<sup>6+</sup>, *ACS Appl. Mater. Interfaces* 14 (2022) 56790–56800, <https://doi.org/10.1021/acsami.2c16923>.
- Q. Wang, Z. Guan, Y. Xiong, D. Li, Nanoconfinement-enhanced Fenton-like polymerization via hollow hetero-shell carbon for reducing carbon emissions in organic wastewater purification, *J. Colloid Interface Sci.* 634 (2023) 231–242, <https://doi.org/10.1016/j.jcis.2022.12.030>.
- J. Qian, H. Wu, F. Wang, A generalized Knudsen theory for gas transport with specular and diffuse reflections, *Nat. Commun.* 14 (2023) 7386, <https://doi.org/10.1038/s41467-023-43104-6>.
- Y. Sheng, X. Wang, Z. Xing, X. Chen, X. Zou, X. Lu, Highly active and chemoselective reduction of halogenated nitroarenes catalyzed by ordered mesoporous carbon supported platinum nanoparticles, *ACS Sustain. Chem. Eng.* 7 (2019) 8908–8916, <https://doi.org/10.1021/acssuschemeng.9b00948>.
- J. Liu, J. Liao, K. Huang, J. Dong, G. He, Z. Gong, H. Fei, A general strategy to remove metal aggregates toward metal–nitrogen–carbon catalysts with exclusive atomic dispersion, *Adv. Mater.* n/a (2023) 2211398, <https://doi.org/10.1002/adma.202211398>.
- J. Ko, R. Berger, H. Lee, H. Yoon, J. Cho, K. Char, Electronic effects of nanoconfinement in functional organic and inorganic materials for optoelectronics, *Chem. Soc. Rev.* 50 (2021) 3585–3628, <https://doi.org/10.1039/D0CS01501F>.
- C.J. Oluigbo, M. Xie, N. Ullah, S. Yang, W. Zhao, M. Zhang, X. Lv, Y. Xu, J. Xie, Novel one-step synthesis of nickel encapsulated carbon nanotubes as efficient electrocatalyst for hydrogen evolution reaction, *Int. J. Hydrg. Energy* 44 (2019) 2685–2693, <https://doi.org/10.1016/j.ijhydene.2018.11.215>.
- Y. Wang, Y. Xie, H. Sun, J. Xiao, H. Cao, S. Wang, Efficient catalytic ozonation over reduced graphene oxide for p-hydroxybenzoic Acid (PHBA) destruction: active site and mechanism, *ACS Appl. Mater. Interfaces* 8 (2016) 9710–9720, <https://doi.org/10.1021/acsami.6b01175>.

[25] C.E. Park, G.H. Jeong, J. Theerthagiri, H. Lee, M.Y. Choi, Moving beyond  $Ti_2C_3T_x$  MXene to Pt-Decorated  $TiO_2@TiC$  core-shell via pulsed laser in reshaping modification for accelerating hydrogen evolution kinetics, *ACS Nano* (2023), <https://doi.org/10.1021/acsnano.2c12638>.

[26] R. Roldán, A.M. Beale, M. Sánchez-Sánchez, F.J. Romero-Salguero, C. Jiménez-Sánchez, J.P. Gómez, G. Sankar, Effect of the impregnation order on the nature of metal particles of bi-functional Pt/Pd-supported zeolite Beta materials and on their catalytic activity for the hydroisomerization of alkanes, *J. Catal.* 254 (2008) 12–26, <https://doi.org/10.1016/j.jcat.2007.10.022>.

[27] S. Jiang, Q. Su, Y. Yin, T. Zhu, X. Li, Extraordinary detoxification effect of arsenic on the cadmium-poisoned  $V_2O_5/TiO_2$  catalyst for selective catalytic reduction of  $NO_x$  by  $NH_3$ , *ACS EST Eng.* (2023), <https://doi.org/10.1021/acs.estengg.2c00418>.

[28] J. Li, X. Lv, B. Wang, M.B.J. Roeffaers, H. Jia, Engineering light propagation for synergistic photo- and thermocatalysis toward volatile organic compounds elimination, *Chem. Eng. J.* 461 (2023) 142022, <https://doi.org/10.1016/j.cej.2023.142022>.

[29] Z. Yang, C. Chen, Y. Zhao, Q. Wang, J. Zhao, G.I.N. Waterhouse, Y. Qin, L. Shang, T. Zhang, Pt Single atoms on CrN nanoparticles deliver outstanding activity and co tolerance in the hydrogen oxidation reaction, *Adv. Mater.* 35 (2023) 2208799, <https://doi.org/10.1002/adma.202208799>.

[30] L. Wang, L. Zhang, W. Ma, H. Wan, X. Zhang, X. Zhang, S. Jiang, J.Y. Zheng, Z. Zhou, In Situ Anchoring Massive Isolated Pt Atoms at Cationic Vacancies of  $\alpha\text{-Ni}_x\text{Fe}_{1-x}\text{OH}_2$  to Regulate the Electronic Structure for Overall Water Splitting, *Adv. Funct. Mater.* 32 (2022) 2203342, <https://doi.org/10.1002/adfm.202203342>.

[31] M. Gao, F. Tian, X. Zhang, Z. Chen, W. Yang, Y. Yu, Improved Plasmonic Hot-Electron Capture in Au Nanoparticle/Polymeric Carbon Nitride by Pt Single Atoms for Broad-Spectrum Photocatalytic  $H_2$  Evolution, *Nano-Micro Lett.* 15 (2023) 129, <https://doi.org/10.1007/s40820-023-01098-2>.

[32] L. Yuan, S. Zeng, G. Li, Y. Wang, K. Peng, J. Feng, X. Zhang, S. Zhang, Low-coordinated single-atom catalysts modulated by metal ionic liquids for efficient  $CO_2$  electroreduction, *Adv. Funct. Mater.* 33 (2023) 2306994, <https://doi.org/10.1002/adfm.202306994>.

[33] Z. Zhou, L. Zhao, J. Wang, Y. Zhang, Y. Li, S. Shoukat, X. Han, Y. Long, Y. Liu, Optimizing  $E_g$  Orbital occupancy of transition metal sulfides by building internal electric fields to adjust the adsorption of oxygenated intermediates for  $Li-O_2$  batteries, *Small* n/a (2023) 2302598, <https://doi.org/10.1002/smll.202302598>.

[34] M. Huang, Y. Li, M. Li, J. Zhao, Y. Zhu, C. Wang, V.K. Sharma, Active site-directed tandem catalysis on single platinum nanoparticles for efficient and stable oxidation of formaldehyde at room temperature, *Environ. Sci. Technol.* 53 (2019) 3610–3619, <https://doi.org/10.1021/acs.est.9b01176>.

[35] Y. Yang, J. Wu, X. Wang, Q. Guo, X. Liu, W. Sun, Y. Wei, Y. Huang, Z. Lan, M. Huang, J. Lin, H. Chen, Z. Wei, Suppressing vacancy defects and grain boundaries via ostwald ripening for high-performance and stable perovskite solar cells, *Adv. Mater.* 32 (2020) 1904347, <https://doi.org/10.1002/adma.201904347>.

[36] R. Zhang, Y. Cao, D.E. Doronkin, M. Ma, F. Dong, Y. Zhou, Single-atom dispersed  $Zn\text{-}N_3$  active sites bridging the interlayer of  $g\text{-}C_3N_4$  to tune NO oxidation pathway for the inhibition of toxic by-product generation, *Chem. Eng. J.* 454 (2023) 140084, <https://doi.org/10.1016/j.cej.2022.140084>.

[37] Z. Liu, Y. Du, R. Yu, M. Zheng, R. Hu, J. Wu, Y. Xia, Z. Zhuang, D. Wang, Tuning mass transport in electrocatalysis down to sub-5 nm through nanoscale grade separation, *Angew. Chem. Int. Ed.* 62 (2023) e202212653, <https://doi.org/10.1002/anie.202212653>.

[38] D. Yi, H. Huang, X. Meng, L. Shi, Adsorption-desorption behavior and mechanism of dimethyl disulfide in liquid hydrocarbon streams on modified Y zeolites, *Appl. Catal. B: Environ.* 148–149 (2014) 377–386, <https://doi.org/10.1016/j.apcatb.2013.11.027>.

[39] C. He, Y. Liao, C. Chen, D. Xia, Y. Wang, S. Tian, J. Yang, D. Shu, Realizing a redox-robust  $Ag\text{/}MnO_2$  catalyst for efficient wet catalytic ozonation of S-VOCs: promotional role of  $Ag(0)\text{/}Ag(I)\text{-}Mn$  based redox shuttle, *Appl. Catal. B: Environ.* 303 (2022) 120881, <https://doi.org/10.1016/j.apcatb.2021.120881>.

[40] Z. Xu, W. Yang, W. Si, J. Chen, Y. Peng, J. Li, A novel  $\gamma$ -like  $MnO_2$  catalyst for ozone decomposition in high humidity conditions, *J. Hazard. Mater.* 420 (2021) 126641, <https://doi.org/10.1016/j.jhazmat.2021.126641>.

[41] M. Keiluweit, P.S. Nico, M.G. Johnson, M. Kleber, Dynamic molecular structure of plant biomass-derived black carbon (Biochar), *Environ. Sci. Technol.* 44 (2010) 1247–1253, <https://doi.org/10.1021/es9031419>.

[42] W. Qu, Z. Tang, W. Liu, Y. Liao, Y. Huang, D. Xia, Q. Lian, S. Tian, C. He, D. Shu, Self-Accelerating Interfacial Catalytic Elimination of Gaseous Sulfur-Containing Volatile Organic Compounds as Microbubbles in a Facet-Engineered Three-Dimensional  $BiOCl$  Sponge Fenton-Like Process, *Environ. Sci. Technol.* 56 (2022) 11657–11669, <https://doi.org/10.1021/acs.est.2c01798>.

[43] Q. Zhou, P. Hong, X. Shi, Y. Li, K. Yao, W. Zhang, C. Wang, J. He, K. Zhang, L. Kong, Efficient degradation of tetracycline by a novel nanoconfinement structure  $Cu_2O\text{/}Cu@MXene$  composite, *J. Hazard. Mater.* 448 (2023) 130995, <https://doi.org/10.1016/j.jhazmat.2023.130995>.

[44] Y. Tan, Q. Zhou, W. Huang, K. Lu, K. Yang, X. Chen, D. Li, D.D. Dionysiou, Highly efficient photocatalytic degradation over rose-like 1D/2D  $La(OH)_3\text{/}(BiO)_2OCl$  heterostructures boosted by rich oxygen vacancies and enhanced interfacial charge transfer, *Environ. Sci.: Nano* 10 (2023) 215–228, <https://doi.org/10.1039/D2EN00792D>.

[45] J. Bing, C. Hu, Y. Nie, M. Yang, J. Qu, Mechanism of catalytic ozonation in  $Fe_2O_3\text{/}Al_2O_3@SBA-15$  aqueous suspension for destruction of ibuprofen, *Environ. Sci. Technol.* 49 (2015) 1690–1697, <https://doi.org/10.1021/es503729h>.

[46] Y. Cheng, B. Wang, P. Yan, J. Shen, J. Kang, S. Zhao, X. Zhu, L. Shen, S. Wang, Y. Shen, Z. Chen, In-situ formation of surface reactive oxygen species on defective sites over N-doped biochar in catalytic ozonation, *Chem. Eng. J.* 454 (2023) 140232, <https://doi.org/10.1016/j.cej.2022.140232>.

[47] S. Zhan, H. Zhang, X. Mi, Y. Zhao, C. Hu, L. Lyu, Efficient Fenton-like Process for Pollutant Removal in Electron-Rich/Poor Reaction Sites Induced by Surface Oxygen Vacancy over Cobalt-Zinc Oxides, *Environ. Sci. Technol.* 54 (2020) 8333–8343, <https://doi.org/10.1021/acs.est.9b07245>.

[48] Z. Ren, Y. Yang, S. Wang, X. Li, H. Feng, L. Wang, Y. Li, X. Zhang, M. Wei, Pt atomic clusters catalysts with local charge transfer towards selective oxidation of furfural, *Appl. Catal. B: Environ.* 295 (2021) 120290, <https://doi.org/10.1016/j.apcatb.2021.120290>.

[49] Y. Wang, J. Xi, X. Duan, W. Lv, H. Cao, C. Chen, Z. Guo, Y. Xie, S. Wang, The duet of surface and radical-based carbocatalysis for oxidative destructions of aqueous contaminants over built-in nanotubes of graphite, *J. Hazard. Mater.* 384 (2020) 121486, <https://doi.org/10.1016/j.jhazmat.2019.121486>.

[50] L. Zhang, X. Li, Y. Chen, H.-T. Wang, Y. Chen, K.H. Chen, Y.-C. Shao, W. Lin, C.-W. Pao, H. Wang, W.-F. Pong, J. Luo, L. Han, Strain-controlled intermetallic  $PtZn$  nanoparticles via N-doping propel highly efficient oxygen reduction electrocatalysis, *ACS Sustain. Chem. Eng.* (2023), <https://doi.org/10.1021/acssuschemeng.3c06146>.

[51] C. He, Y. Wang, Z. Li, Y. Huang, Y. Liao, D. Xia, S. Lee, Facet engineered  $\alpha\text{-MnO}_2$  for efficient catalytic ozonation of  $Odor\text{-}CH_3SH$ : oxygen vacancy-induced active centers and catalytic mechanism, *Environ. Sci. Technol.* 54 (2020) 12771–12783, <https://doi.org/10.1021/acs.est.0c05235>.

[52] P. Peljo, H.H. Girault, Electrochemical potential window of battery electrolytes: the HOMO-LUMO misconception, *Energy Environ. Sci.* 11 (2018) 2306–2309, <https://doi.org/10.1039/C8EE01286E>.

[53] L. Zhu, D. Shen, H. Zhang, K.H. Luo, C. Li, Fabrication of Z-scheme  $Bi_7O_3I_3\text{/}g\text{-}C_3N_4$  heterojunction modified by carbon quantum dots for synchronous photocatalytic removal of  $Cu\text{(VI)}$  and organic pollutants, *J. Hazard. Mater.* 446 (2023) 130663, <https://doi.org/10.1016/j.jhazmat.2022.130663>.

[54] H. Ren, F. Qi, A. Labidi, J. Zhao, H. Wang, Y. Xin, J. Luo, C. Wang, Chemically bonded carbon quantum dots/ $Bi_2WO_6$  S-scheme heterojunction for boosted photocatalytic antibiotic degradation: interfacial engineering and mechanism insight, *Appl. Catal. B: Environ.* (2023) 122587, <https://doi.org/10.1016/j.apcatb.2023.122587>.

[55] T. Zhao, J. Li, J. Liu, F. Liu, K. Xu, M. Yu, W. Xu, F. Cheng, Tailoring the Catalytic Microenvironment of  $Cu_2O$  with  $SiO_2$  to Enhance  $C_2^{+}$  Product Selectivity in  $CO_2$  Electroreduction, *ACS Catal.* 13 (2023) 4444–4453, <https://doi.org/10.1021/acscatal.3c00056>.

[56] M. Gao, L. Wang, Y. Yang, Y. Sun, X. Zhao, Y. Wan, Metal and Metal Oxide Supported on Ordered Mesoporous Carbon as Heterogeneous Catalysts, *ACS Catal.* 13 (2023) 4060–4090, <https://doi.org/10.1021/acscatal.2c05894>.